Robust Registration by Rank Minimization for Multiangle Hyper/Multispectral Remotely Sensed Imagery

Ting Hu, Hongyan Zhang, *Member*, *IEEE*, Huanfeng Shen, *Senior Member*, *IEEE*, and Liangpei Zhang, *Senior Member*, *IEEE*

Abstract—**Multiangle images are acquired over roughly the same earth surface from different angles, and accurate image registration is a key prerequisite for their application. In this paper, we propose a robust registration method by rank minimization (RRRM) for multiangle hyper/multispectral remotely sensed imagery (MA-HSI-MSI). First, the low-rank structure of the MA-HSI-MSI is exploited and utilized as the registration constraint, thus recasting the image registration problem as searching for an optimal set of transformations, such that the matrix of the transformed images can reach its minimum rank. Second, a patch-based registration scheme is adopted to solve the problem of inconsistent geometric distortion over the entire image, taking the homography model as the local transformation. An iterative convex optimization algorithm is then used to solve the rank minimization-based image registration model for each image patch. Finally, all the transformed patches are used to synthesize the final registration image. The experimental results demonstrate that the proposed low-rank registration method works effectively for CHRIS/Proba imagery and WorldView-2 imagery.**

Index Terms—**Hyper/multispectral, image registration, multiangle, rank minimization.**

I. INTRODUCTION

MULTIANGLE remote sensing sensors retrieve the directional reflectance properties of the earth's surface, which open up new applications in the retrieval of physical scene characteristics, as well as quantitative improvements in classification accuracy through image fusion and resolution enhancement [1]–[3]. Many recently launched imaging systems are equipped with multiangle capabilities, including the Multispectral Thermal Imager (MTI), the Multiangle Imaging Spectroradiometer (MISR), the Along Track Scanning Radiometers (ATSR-1, ATSR-2, and AATSR), the Compact High Resolution Imaging Spectrometer (CHRIS) onboard the Project for On-Board Autonomy (Proba) satellite [4], [5], and WorldView-2. However, for all of the successful applications of multiangle imagery, accurate registration of the multiple-view images, which at times are also multitemporal, is a prerequisite [6].

Generally speaking, image registration can be divided into three steps: 1) preparation of a sufficient number of control points (CPs); 2) estimation of the mapping function between the images to be registered using the CPs; and 3) resampling of the images for alignment with the reference system, using the mapping function [7]. Of these three steps, the first step is the most important because it directly determines how well the transformation can be estimated by the next two steps. One of the important applications when detecting CPs is to establish correspondences or to measure the similarity among different images. Therefore, the detected points should be stable or invariant under transformations incurred by changes in viewpoint or illumination. In the past decades, numerous invariant features and descriptors have been proposed, studied, compared, and tuned [8]. Among the feature descriptors, scale-invariant feature transform (SIFT) has been widely used, and is, to a large extent, invariant to changes in rotation, scale, and illumination [9]. Nevertheless, if the images are taken from very different viewpoints, SIFT may fail to establish enough reliable correspondences, and its affine-invariant version (Affine-SIFT) was proposed to obtain more correspondences, but suffers from low accuracy [10].

However, these traditional feature descriptors cannot work well when applied to multiangle remote sensing images. For images with large view angles, the existence of resolution change and blurring makes the precise location of CPs difficult. In addition, local geometric distortion caused by topographic effects and/or platform instability means that no global rigid transformation models are appropriate, which forms another challenge for the multiangle image registration [11]. Due to these two problems, only a few methods can achieve promising registration accuracy, especially for large view angle images. In [12], an effective method using a physical sensor model is elaborated; however, the availability of a DEM, as well as reliable metadata on sensor geometry, is required. Unfortunately, this cannot always be obtained, especially for certain imaging systems [4]. For example, for CHRIS/Proba imagery, reliable determination of satellite-target geometry poses some difficulties. In addition, the method proposed in [12] can only be described as semi-automatic, as manual CP collection needs to be undertaken in the case where the area of overlap between the input and orthorectified images is limited. Recently, a two-step nonrigid automatic registration scheme for multiangle

Manuscript received July 12, 2013; revised March 05, 2014; accepted March 08, 2014. Date of publication March 25, 2014; date of current version August 01, 2014. This work was supported in part by the National Basic Research Program of China (973 Program) under Grant 2011CB707105, in part by the 863 program under Grant 2013AA12A301, and in part by the National Natural Science Foundation of China under Grant 61201342. *(Corresponding author: H. Zhang.)*

T. Hu, H. Zhang, and L. Zhang are with the State Key Laboratory of Information Engineering in Surveying, Mapping, and Remote Sensing, Wuhan University, Wuhan 430079, China (e-mail: zhanghongyan@whu.edu.cn).

H. Shen is with the School of Resource and Environmental Science, Wuhan University, Wuhan, China.

Color versions of one or more of the figures in this paper are available online at http://ieeexplore.ieee.org.

Digital Object Identifier 10.1109/JSTARS.2014.2311585

CHRIS/Proba satellite images was proposed in [13]. In the first step, CPs are selected in a preregistration process based on the SIFT features. In the second step, the preliminary registered image is then divided into chips of 64×64 pixels, and each chip is matched with a corresponding chip in the reference image, using normalized cross-correlation (NCC). Selected SIFT and NCC CPs are then used to define a nonrigid thin-plate-spline model. The two challenges mentioned above are considered in this method, but it may not work when no SIFT CPs can be found in the first step [14], which may often be the case for large view angle image registration. Furthermore, the two consecutive resampling procedures may cause a change of pixel profile, leading to a loss of image details.

The repeatability of feature extraction and the correctness of feature matching remain issues in the presence of severe clutter and challenging viewing conditions [15]. Viewpoint changes considerably lower the probability of detecting consistent features in different images (features that capture the same physical surface but may appear different due to viewpoint change) [16]. Large view angle images are often affected by illumination difference from the nadir image, which leads to an insufficient number of extracted features. From this perspective, making use of feature descriptors cannot achieve satisfactory results in multiangle remote sensing imagery registration. Furthermore, with the feature points-based image registration method, only one remotely sensed angle image can be registered with respect to the reference nadir image in a single registration procedure. When all the different angle images are required in the application, the image registrations for each angle image must be performed separately, which may cause error transfer or accumulation.

In recent years, with the rapid development of matrix rank-related optimization techniques, low-rank structure has become an effective constraint for various data registration tasks [17]–[19], including face images, seismogram data, and so on, and has achieved impressive performances. In [17], Peng *et al.* discussed the low-rank structure of a batch of correlated natural images, and formulated the batch image alignment problem as the search for a set of transformations that minimizes the rank of the transformed images. In addition, Wang *et al.* [18] performed automatic misalignment correction of seismograms with the low-rank structure of the seismogram data. Wu *et al.* [19] studied the problem of online alignment of a newly arrived image to previously well-aligned images by identifying the low-rank component of the well-aligned image basis. Unlike the traditional feature-based image registration methods, the success of these rank-based data alignment methods can mainly be attributed to the identification of the low-rank structure of the processed data as the effective constraint. Therefore, for multiangle hyper/multispectral imagery (MA-HSI-MSI), the main task is to exploit the low-rank structure of the MA-HSI-MSI and apply it in the formulation of the rank minimization-based MA-HSI-MSI registration model. To the best of our knowledge, in the literature to date, there have not been any registration methods developed for remote sensing images which use the low-rank structure.

In view of this, we propose a robust registration method by rank minimization (RRRM) for MA-HSI-MSI. The method is fully automatic and does not require any prior knowledge of the sensor geometry. First, the low-rank structure of the MA-HSI-MSI is exploited and utilized as the image feature for the image registration, which enables us to build a rank minimization-based MA-HSI-MSI registration model that is solved by an iterative convex optimization method. Second, a patch-based registration scheme, which treats each local image patch with a rigid transformation model, is utilized to tackle the problem of inconsistency of the entire image transformation model. The main contribution of this paper is that all the bands of the multiangle images participate in the image registration procedure at the same time, which improves the image registration performance and the robustness to stripe noise and occlusions. The experimental results with CHRIS/Proba and WorldView-2 images confirm the effectiveness of the proposed MA-HSI-MSI registration method.

The structure of the paper is as follows. In Section II, we explain the low-rank structure of MA-HSI-MSI. In Section III, we formulate the image registration problem as a matrix rank minimization problem and we describe the iterative convex optimization algorithm. We then summarize the whole flowchart of the MA-HSI-MSI registration scheme. In Section IV, the experimental results with CHRIS/Proba and WorldView-2 images, and the corresponding experimental analysis, are provided. Finally, Section V concludes the paper with a discussion of the different directions of our future work.

II. THE LOW-RANK STRUCTURE OF MA-HSI-MSI

MA-HSI-MSI can provide us with sufficient measurements of the same surface, from both the angular and the spectral perspective. Generally speaking, there is a high correlation between these measurements, which allows for the low-rank property of MA-HSI-MSI.

First, we exploit the low-rank property of single-angle hyperspectral imagery (HSI) from the qualitative and quantitative perspectives, respectively. Qualitatively, high correlations exist for HSI, both spatially and spectrally, which means that efficient compression algorithms can be designed to reduce the huge size and allow for convenient data storage and transfer. Furthermore, the principal component analysis (PCA) transformation can reduce the dimension of HSI data to a few principal components in practical applications [20], [21] such as classification, target detection, and so on. All these facts reveal one important truth: that the data structure of HSI is low rank.

The low-rank structure of a clean hyperspectral image can also be explored quantitatively from the perspective of the linear mixing model [22]–[24]. By lexicographical rearrangement, a hyperspectral image with n bands can be represented as a 2-D matrix $\mathbf{X} \in \mathbb{R}^{m \times n}$, where m represents the number of image pixels. Here, the jth column $\mathbf{X}_j$ denotes the lexicographically reshaped jth band of the hyperspectral image. There are high correlations between the hyperspectral pixels (rows of $\mathbf{X}$), as each pixel can be decomposed as the combination of several endmembers. Assuming that the observation region is composed of ρ different endmembers, let $\mathbf{S} \in \mathbb{R}_+^{n \times \rho}$ be the matrix whose columns contain the spectral signatures of these materials along n frequency bands, and let $\mathbf{A} \in \mathbb{R}_+^{m \times \rho}$ be the matrix containing the fraction of the corresponding endmembers, i.e., $\mathrm{A}_{i,j}$ indicates the percentage of the jth endmember in pixel i. Therefore, the whole HSI matrix can be factorized into $\mathbf{X} = \mathbf{A}\mathbf{S}^{\mathrm{T}}$, which is known as the linear mixture model [25]. As the value of ρ is usually relatively small, i.e., $\rho \ll \min(m, n)$, the rank of $\mathbf{X}$ is bounded, which suggests the low-rank structure of $\mathbf{X}$.

All the angle images of the same earth surface can be denoted as $\mathbf{X}_0, \mathbf{X}_1, \ldots, \mathbf{X}_s \in \mathbb{R}^{m \times n}$, where $s + 1$ denotes the number of angles. Each angle image has a size of m pixels and n bands. Initially, these angle images are not well registered. Let $\mathbf{X}_0$ represent the reference nadir image, and the others, $\mathbf{X}_1, \ldots, \mathbf{X}_s$, are the input images to be registered. Clearly, all the bands of the same angle image will suffer from the same distortion, so s groups of transformation parameters for all the angle images need to be estimated. If we find the optimal transformations $\mathbf{H}_1, \ldots, \mathbf{H}_s$ among them, they can be transformed into the coordinate system of the reference image, and become well registered. The well-registered MA-HSI-MSI can then be expressed as

$$\mathbf{A} = [\mathbf{X}_0 | \mathbf{X}_1 \circ \mathbf{H}_1 | \cdots | \mathbf{X}_s \circ \mathbf{H}_s] \in \mathbb{R}^{m \times ((s+1) \times n)}. \quad (1)$$

As shown in [17], if $\mathbf{X}_0, \mathbf{X}_1, \ldots, \mathbf{X}_s$ are of some convex Lambertian object under varying illumination and viewpoints, then a rank-9 approximation suffices. Therefore, even for multispectral images, with the help of the multiangle capability, sufficient measurements can be obtained. Therefore, the $s + 1$ well-registered MA-HSI-MSI should be low rank. Image registration can be viewed as the identification of this low-rank structure.

III. ROBUST IMAGE REGISTRATION BY RANK MINIMIZATION

In this section, we first formulate the image registration as the search for a set of transformations that minimizes the rank of the transformed images. An iterative convex optimization method is then introduced in detail to solve the transformation parameters. Finally, we provide the flowchart for the MA-HSI-MSI registration.

A. Modeling Registration as Domain Transformation

Domain transformations are usually used for geometric correction and registration. In the work of Ma *et al.* [26], affine transformation was adopted to describe the image deformation. In fact, homography transformation is more suitable for viewpoint changes [8], so we choose homography transformation to describe the multiangle image geometric distortion.

Suppose the point in the image to be registered is denoted by $Q(x, y)$, then we use $P(x', y')$ to represent the corresponding point in the reference image. The homography transformation $\mathbf{H} = [h_{ij}](i, j = 1, 2, 3)$ can be derived by the following equation [27]:

$$\begin{bmatrix} x' \\ y' \\ 1 \end{bmatrix} = \begin{bmatrix} h_{11} & h_{12} & h_{13} \\ h_{21} & h_{22} & h_{23} \\ h_{31} & h_{32} & h_{33} \end{bmatrix} \begin{bmatrix} x \\ y \\ 1 \end{bmatrix}. \quad (2)$$

Due to the scale variability of the homography matrix, h_{33} is normalized to 1, and then only eight parameters are independent of each other. We now take all the angle images and let $\mathbf{X}_{i,j} (i = 0, \ldots, s; j = 1, \ldots, n)$ denote the jth band of the ith angle image. Here, we select the nadir image $\mathbf{X}_0$ as the reference image, and our goal is to make the other angle images, $\mathbf{X}_1, \ldots, \mathbf{X}_s$, registered to the reference one. In other words, we need to find s groups of transformations $\mathbf{H}_1, \ldots, \mathbf{H}_s$ and each group will have eight degrees of freedom. Therefore, the transformed images $\mathbf{X}_1 \circ \mathbf{H}_1, \ldots, \mathbf{X}_s \circ \mathbf{H}_s$ will be well aligned at the pixel level or, equivalently, the matrix

$$\mathbf{D} \circ \mathbf{H} = [\mathbf{X}_0 | \mathbf{X}_1 \circ \mathbf{H}_1 | \cdots | \mathbf{X}_s \circ \mathbf{H}_s] \in \mathbb{R}^{m \times ((s+1) \times n)} \quad (3)$$

is low rank, where $\mathbf{D}$ denotes all the multiangle observations, and $\mathbf{H}$ is a general term for all the transformation parameters. The multiangle image registration can therefore be reduced to the following optimization problem:

$$\min_{\mathbf{A}, \mathbf{H}} rank(\mathbf{A}) \quad s.t. \mathbf{D} \circ \mathbf{H} = \mathbf{A}. \quad (4)$$

Thus, the registration of the MA-HSI-MSI can be transformed to solve the set of transformations $\mathbf{H}$ by optimizing the rank minimization problem (4).

However, the low-rank structure of the registered images can be easily violated due to the presence of noise, partial corruptions, and occlusions, which are caused by the multiangle imaging. Since these errors usually occupy only a small amount of the whole image, we can model them as sparse errors whose non-zero entries can have arbitrarily large magnitudes [28].

Let $\mathbf{E} = \{e_{i,j}\}$ represent the large and sparse errors in the image $\mathbf{X}_{i,j}$, then we can modify (4) to the following:

$$\min_{\mathbf{A}, \mathbf{E}, \mathbf{H}} rank(\mathbf{A}) \quad \text{s.t.}\, \mathbf{D} \circ \mathbf{H} = \mathbf{A} + \mathbf{E},\ \|\mathbf{E}\|_0 \leq k \quad (5)$$

where the $\ell_0 - norm \; \|\bullet\|_0$ counts the number of non-zero entries in the sparse error matrix $\mathbf{E}$, and k is a constant that represents the maximum number of corrupted pixels. The Lagrangian form of this problem is more convenient to solve

$$\min_{\mathbf{A}, \mathbf{E}, \mathbf{H}} rank(\mathbf{A}) + \gamma \|\mathbf{E}\|_0 \quad \text{s.t.}\, \mathbf{D} \circ \mathbf{H} = \mathbf{A} + \mathbf{E} \quad (6)$$

where $\gamma > 0$ is a weighting parameter that trades off the rank of the solution versus the sparsity of the error.

Here, we only consider sparse large-magnitude errors in images in (6). In fact, real images are unavoidably corrupted by additive Gaussian noise in all the pixels. Fortunately, it has been proved that the sparse and low-rank matrix decomposition is stable to additive Gaussian noise of a small magnitude, in addition to sparse errors [29]. Thus, the optimization model can be modified as follows:

$$\min_{\mathbf{A}, \mathbf{E}, \mathbf{H}} rank(\mathbf{A}) + \gamma \|\mathbf{E}\|_0 \quad \text{s.t.}\, \|\mathbf{D} \circ \mathbf{H} - \mathbf{A} - \mathbf{E}\|_F \leq \varepsilon \quad (7)$$

where $\varepsilon > 0$ is the noise level.

B. Solution by Iterative Convex Optimization

The optimization problem shown in (7) is not, however, directly tractable, because both the rank and the ℓ_0 norm are nonconvex and discontinuous, and the constraint is highly nonlinear with respect to $\mathbf{H}$. In this section, we introduce an effective practical solution to this problem, building on recent advances in algorithms for robust matrix rank minimization.

It has been shown that for the problem of recovering low-rank matrices from sparse errors [30], the rank function *rank*($\mathbf{A}$) and the ℓ_0 norm $\|\mathbf{E}\|_0$ can be replaced by the matrix nuclear norm $\|\mathbf{A}\|_*$ and the ℓ_1 norm $\|\mathbf{E}\|_1$. Here, $\|\mathbf{A}\|_* = \sum_{i=1}^{\min\{m,(s+1)\times n\}} \sigma_i(\mathbf{A})$, i.e., the sum of the singular values, and $\|\mathbf{E}\|_1 = \sum_{ij} |\mathbf{E}_{ij}|$. Thus, we get the following optimization problem:

$$\min_{\mathbf{A},\mathbf{E},\mathbf{H}} \|\mathbf{A}\|_* + \gamma\|\mathbf{E}\|_1 \quad \text{s.t.}\ \|\mathbf{D} \circ \mathbf{H} - \mathbf{A} - \mathbf{E}\|_F \le \varepsilon. \tag{8}$$

We now get a convex objective function, but the constraint is nonlinear with respect to the homography transformation $\mathbf{H}$, which makes the whole optimization problem not convex. When the change of $\mathbf{H}$ is small, we can approximate the constraint by linearizing the current estimate of $\mathbf{H}$. We now identify the transformation $\mathbf{H} = [\mathbf{H}_1|\ldots|\mathbf{H}_S] \in \mathbb{R}^{8\times s}$, and we have s groups to estimate, with each group having eight parameters. For an initial value $\mathbf{H}^0$, when the change $\Delta\mathbf{H} = [\Delta\mathbf{H}_1|\ldots|\Delta\mathbf{H}_s] \in \mathbb{R}^{8\times s}$ is small enough, we can use the Taylor expansion, i.e., $\mathbf{D} \circ (\mathbf{H}^0 + \Delta\mathbf{H}) \approx \mathbf{D} \circ \mathbf{H}^0 + \sum_{i=1}^{s} \mathbf{J}_i \Delta\mathbf{H}_i \boldsymbol{\varepsilon}_i^T$, where $\mathbf{J}_i = \frac{\partial}{\partial\boldsymbol{\zeta}}(\mathbf{X}_i \circ \boldsymbol{\zeta})|_{\boldsymbol{\zeta}=\mathbf{H}_i} \in \mathbb{R}^{m\times 8}$ is the Jacobian of the ith angle image, with respect to the transformation parameters $\mathbf{H}_\mathrm{i}$, and $\{\boldsymbol{\varepsilon}_i\}$ denotes the standard basis for $\mathbb{R}^s$. The convex optimization problem with respect to the unknowns $\mathbf{A}$, $\mathbf{E}$, and $\Delta\mathbf{H}$ now becomes

$$\min_{\mathbf{A},\mathbf{E},\Delta\mathbf{H}} \|\mathbf{A}\|_* + \gamma\|\mathbf{E}\|_1 \ \ \text{s.t.}\, \mathbf{D} \circ \mathbf{H}^0 + \sum_{i=1}^{s} \mathbf{J}_i \Delta\mathbf{H}_i \boldsymbol{\varepsilon}_i^T = \mathbf{A} + \mathbf{E}. \tag{9}$$

The linearization procedure only holds locally, so we should solve (8) by repeatedly linearizing about our current estimate of $\mathbf{H}$ and iteratively performing a sequence of convex programs of the form of (9). The implementation details of the proposed image registration algorithm for MA-HSI-MSI are shown in Algorithm 1. The algorithm stops when the relative change of the cost function between two consecutive iterations is less than the predetermined threshold. Details of the convergence analysis can be found in [31]–[33].

The main computational cost in Algorithm 1 at each iteration is the third step, which solves the linearized convex optimization problem (9). This part can be efficiently solved by a first-order method, the Augmented Lagrange Multiplier (ALM) algorithm. The basic idea of the ALM algorithm is to search for a saddle point of the augmented Lagrangian function. The augmented Lagrangian function is formulated as

$$\begin{aligned} L_\mu(\mathbf{A}, \mathbf{E}, \Delta\mathbf{H}, \mathbf{Y}) = \|\mathbf{A}\|_* + \gamma\|\mathbf{E}\|_1 + \langle \mathbf{Y}, h(\mathbf{A}, \mathbf{E}, \Delta\mathbf{H})\rangle \\ + \frac{\mu}{2}\|(\mathbf{A}, \mathbf{E}, \Delta\mathbf{H})\|_F^2 \end{aligned} \tag{10}$$

where $h(\mathbf{A}, \mathbf{E}, \Delta\mathbf{H}) = \mathbf{D} \circ \mathbf{H} + \sum_{i=1}^{S} \mathbf{J}_i \Delta\mathbf{H}_i \boldsymbol{\varepsilon}_i^T - \mathbf{A} - \mathbf{E}$, $\mathbf{Y} \in \mathbb{R}^{m^*4}$ is a Lagrange multiplier matrix, $\langle\cdot,\cdot\rangle$ denotes the matrix inner product, i.e., $\langle \mathbf{X}, \mathbf{Y}\rangle = trace(\mathbf{X}^T\mathbf{Y})$, μ is a positive scalar, and $\|\cdot\|_\mathrm{F}$ represents the Frobenius norm. If we choose the appropriate matrix $\mathbf{Y}$ and a sufficiently large constant μ, the augmented Lagrangian function has the same minimizer as the original constrained optimization problem. The ALM algorithm iteratively estimates both the Lagrange multiplier and the optimal solution by iteratively minimizing the augmented Lagrangian function

$$\begin{aligned} (\mathbf{A}_{k+1}, \mathbf{E}_{k+1}, \Delta\mathbf{H}_{k+1}) &= \arg\min_{A,E,\Delta H} L_{\mu_k}(\mathbf{A}, \mathbf{E}, \Delta\mathbf{H}, \mathbf{Y}_k) \\ \mathbf{Y}_{k+1} &= \mathbf{Y}_k + \mu_k h(\mathbf{A}_{k+1}, \mathbf{E}_{k+1}, \Delta\mathbf{H}_{k+1}). \end{aligned} \tag{11}$$

The first step is difficult to solve directly. One method is to minimize the Lagrangian function by adopting an alternating scheme, optimizing one parameter while fixing the others

$$\begin{aligned} \mathbf{A}_{k+1} &= \arg\min_{\mathbf{A}} L_{\mu_k}(\mathbf{A}, \mathbf{E}_{k+1}, \Delta\mathbf{H}_k, \mathbf{Y}_k) \\ \mathbf{E}_{k+1} &= \arg\min_{\mathbf{E}} L_{\mu_k}(\mathbf{A}_{k+1}, \mathbf{E}, \Delta\mathbf{H}_k, \mathbf{Y}_k) \\ \Delta\mathbf{H}_{k+1} &= \arg\min_{\Delta\mathbf{H}} L_{\mu_k}(\mathbf{A}_{k+1}, \mathbf{E}_{k+1}, \Delta\mathbf{H}, \mathbf{Y}_k). \end{aligned} \tag{12}$$

To spell out the solutions, the operator for the scalars is defined as follows:

$$S_\tau[x] = sign(x) \cdot \max\{|x| - \tau, 0\} \tag{13}$$

where $\tau \ge 0$. When applied to the vector or matrix, the operator acts element-wise. Therefore, we can rewrite the problem as

$$\begin{aligned} (\mathbf{U}, \boldsymbol{\Sigma}, \mathbf{V}) &= \mathrm{svd}\left(\mathbf{D} \circ \mathbf{H} + \sum_{i=1}^{s} \mathbf{J}_i \Delta\mathbf{H}_i \boldsymbol{\varepsilon}_i^T + \frac{1}{\mu_k}\mathbf{Y}_k - \mathbf{E}_k\right) \\ \mathbf{A}_{k+1} &= \mathbf{U} S_{1/\mu_k}[\boldsymbol{\Sigma}]\mathbf{V}^T \\ \mathbf{E}_{k+1} &= S_{1/\mu_k}\left[\mathbf{D} \circ \mathbf{H} + \sum_{i=1}^{s} \mathbf{J}_i \Delta\mathbf{H}_i \boldsymbol{\varepsilon}_i^T + \frac{1}{\mu_k}\mathbf{Y}_k - \mathbf{A}_{k+1}\right] \\ \Delta\mathbf{H}_{k+1} &= \sum_{i=1}^{s} \mathbf{J}_i^\dagger \left(\mathbf{A}_{k+1} + \mathbf{E}_{k+1} - \mathbf{D} \circ \mathbf{H} - \frac{1}{\mu_k}\mathbf{Y}_k\right)\boldsymbol{\varepsilon}_i^T \end{aligned} \tag{14}$$

where svd($\cdot$) denotes the singular value decomposition operator, and $\mathbf{J}_i^\dagger$ denotes the Moore-Penrose pseudo-inverse of $\mathbf{J}_i$.

C. The Flowchart of the RRRM Method for MA-HSI-MSI

Considering the issue of local distortion in multiangle images, a patch-based registration scheme is chosen. This scheme treats each local image patch with a rigid transformation model, but globally the model is nonrigid to tackle the problem of inconsistency of the entire image transformation model. Both the input images and the reference image are first divided into patches with a certain degree of overlap. Each patch is stacked as a vector to find the local transformation parameters that make the matrix rank obtain its minimum, and then all the registered patches are synthesized to obtain the whole registered image. Suppose the image has a size of $M \times N$ pixels, then we choose $p \times q$ as the size of each patch and move the patch across the reference image, with an overlap of t pixels between each adjacent patch. Thus, the proposed method performs as the following Algorithm 2.

Algorithm 1

```
Input: Multiangle images $\mathbf{X}_0, \mathbf{X}_1, \ldots, \mathbf{X}_s \in \mathbb{R}^{m\times n}$ the initial homography transformation parameters $\mathbf{H}_1^0, \ldots, \mathbf{H}_s^0$ for each angle image, and the weighting parameter $\gamma > 0$.
Initialization:
1) Normalize images $(\mathbf{X}_{i,j} \circ \mathbf{H}_i)/\|(\mathbf{X}_{i,j} \circ \mathbf{H}_i)\|_2$ in order to rule out the trivial solutions such as zooming in on a single dark pixel or a dark region in the image.
2) Iteration number $k = 0$.
While not converged Do
    1) Compute the Jacobian matrices w.r.t. transformation $\mathbf{H}_i^k$:
        $$\mathbf{J}_i^k \leftarrow \frac{\partial}{\partial \zeta}\left(\frac{\mathbf{X}_i \circ \boldsymbol{\zeta}}{\|\mathbf{X}_i \circ \boldsymbol{\zeta}\|_2}\right)_{|\zeta = \mathbf{H}_i^k}, \quad i = 1, \ldots, s$$
    2) Warp the images:
        $$\mathbf{D} \circ \mathbf{H}^k \leftarrow \left[\frac{\mathbf{X}_1 \circ \mathbf{H}_1^k}{\|\mathbf{X}_1 \circ \mathbf{H}_1^k\|_2} | \ldots | \frac{\mathbf{X}_S \circ \mathbf{H}_s^k}{\|\mathbf{X}_S \circ \mathbf{H}_s^k\|_2}\right]$$
    3) Solve the linearized convex optimization by an iterative process:
        $$(\mathbf{A}^*, \mathbf{E}^*, \Delta\mathbf{H}^{k*}) \leftarrow \min_{\mathbf{A},\mathbf{E},\Delta\mathbf{H}} \|\mathbf{A}\|_* + \gamma\|\mathbf{E}\|_1$$
        $$s.t.\, \mathbf{D} \circ \mathbf{H}^k + \sum\nolimits_{i=1}^{s} \mathbf{J}_i^k \Delta\mathbf{H}_i^k \boldsymbol{\varepsilon}_i^T = \mathbf{A} + \mathbf{E};$$
    4) Update transformations: $\mathbf{H}^{k+1} \leftarrow \mathbf{H}^k + \Delta\mathbf{H}^{k*}$ and the iteration number $k = k + 1$
End While
Output: Solution $\mathbf{A}^*$, $\mathbf{E}^*$ and the whole change of $\mathbf{H}$ with respect to $\mathbf{H}^0$: $\Delta\mathbf{H}^* = \sum_k \Delta\mathbf{H}^{k*}$.
```

Algorithm 2

```
Input: A dataset of MA-HSI-MSI, including one nadir image and other angle images.
Initialization
1) Use a traditional feature extraction operator, Harris, for example, to get the initial homography transformation parameters $\mathbf{H}_1^0, \ldots, \mathbf{H}_s^0$ for each angle image.
2) Both the nadir image and the angle images are divided into patches with respect to the initial homography transformation, with a certain degree of overlap.
3) Each nadir patch and its corresponding angle image patches are viewed as an image patch set.
Main steps
1) For each patch set, the nadir patch and the other angle patches are referred to as $\mathbf{X}_0, \mathbf{X}_1, \ldots, \mathbf{X}_s \in \mathbb{R}^{m\times n}$.
2) Solve the transformation parameters among $\mathbf{X}_0, \mathbf{X}_1, \ldots, \mathbf{X}_s$ via Algorithm 1.
3) Warp the input patches according to the solution sought out in step 2.
4) Turn to the next set of patches and repeat the above three steps until all the sets are dealt with.
5) Synthesize all the registered patches into the whole image.
Output: In order to obtain spatially consistent results, overlapping parts of patches are fused by averaging, and a full image is obtained.
```

IV. EXPERIMENTS AND ANALYSIS

A. Experiment Data and Quantitative Evaluation Factors

In the experimental section, CHRIS/Proba and WorldView-2 images are chosen to represent the multiangle hyperspectral and multispectral images, respectively. First, we make a brief introduction to these two types of images.

1) CHRIS/Proba Imagery: The spaceborne ESA-mission CHRIS/Proba provides hyperspectral and multidirectional data of selected targets spread all over the world. CHRIS/Proba provides multiple observations of the same scene at five different angles ($+55°$, $+36°$, $0°$, $-36°$, and $-55°$). In addition, each angle image has multiple bands, and the number of bands differs in different modes. For example, for Mode 3, which is mainly used for land observation, each angle image has 18 bands, together forming 90 bands for five angles, which reveals the multiangle and hyperspectral property of the CHRIS/Proba imagery. Detailed information about CHRIS/Proba imagery is provided in Table I [32].

To save space, we select one dataset of images from Mode 2, Mode 3, and Mode 5, respectively, as representatives to conduct the experiments. According to their corresponding areas, they are termed CHRIS_FY, CHRIS_UK, and CHRIS_BA. Detailed descriptions of the utilized images are provided in Table II. The five selected CHRIS/Proba images are shown in Figs. 1–3, respectively. All the CHRIS/Proba images were preprocessed with the open-source BEAM CHRIS-Box software [34], which includes two important procedures: 1) noise reduction, i.e., the replacement of missing data and destriping; and 2) atmospheric correction, i.e., the retrieval of the surface reflectance from remotely sensed imagery by removing the atmospheric effects [35]. In fact, noise or other distortions may still exist after the preprocessing, e.g., some bands cannot be filtered completely. Some of these situations can be seen in Fig. 4, where band 2 of CHRIS_FY still suffers from severe stripe noise, and there are some occlusions in band 3 of CHRIS_BA, due to the topography variation.

2) WorldView-2 Imagery: WorldView-2 was launched in late 2009, and provides commercially available panchromatic imagery at 0.5 m resolution, and 8-band multispectral imagery at 1.8 m resolution. The eight bands of the multispectral image refer to coastal, blue, green, yellow, red, red edge, near-IR1, and near-IR2. The sensor acquires different angle images at 44.7°, 56.0°, and 81.4° in the forward direction, and 59.8° and 44.6° in the backward direction.

TABLE I
INFORMATION ABOUT CHRIS/PROBA IMAGERY

	Mode 1	Mode 2	Mode 3	Mode 4	Mode 5
Band number	62	18	18	18	37
Band range (nm)	406–992	406–1003	438–1035	486–788	438–1003
Band width (nm)	6–20	6–33	6–33	6–11	6–33
Resolution nadir (m)	34	17	17	17	17
Application	Agriculture	Water	Land	Chlorophll	Land

TABLE II
DETAILED INFORMATION ABOUT THE UTILIZED IMAGES

	Scene description	Acquisition date	Spatial resolution	Image size
CHRIS_FY	Fethiye (Turkey)	02-12-2009	17 m	748×744
CHRIS_UK	Lena Delta (Russia)	23-07-2008	17 m	748×744
CHRIS_BA	Baasdorf (Germany)	24-04-2009	17 m	370×748
WV-2	Rio de Janeiro (Brazil)	19-01-2010	1.8 m	400×400

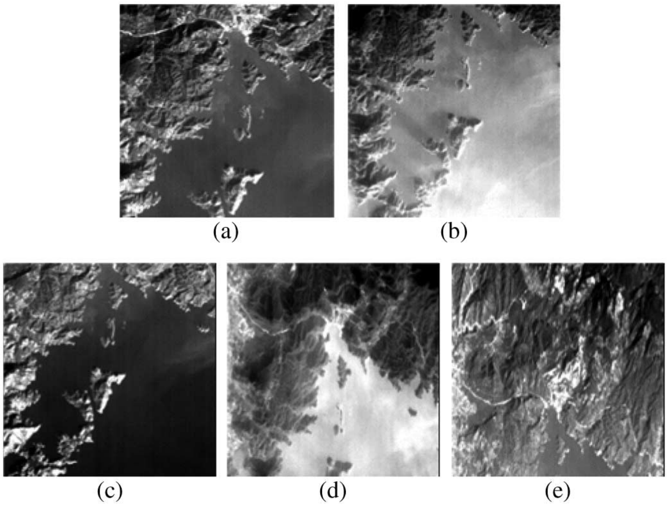
(a) (b)
(c) (d) (e)

Fig. 1. Band 4 of CHRIS_FY (Mode 2) MA-HSI. From (a) to (e): fly-zenith angles are $0°$, $+36°$, $-36°$, $+55°$, and $-55°$.

Here, the WorldView-2 image data which was provided by DigitalGlobe for the purpose of the 2011 GRSS Data Fusion Contest is utilized to validate the performance of the proposed RRRM method. This data covers Santos Dumont Airport of Rio de Janeiro city, Brazil. A subregion composed of 400×400 pixels, as shown in Fig. 5, was cropped as the study area and is termed WV-2. Detailed information about the utilized image set is provided in Table II.

3) Quantitative Evaluation Factors: In order to evaluate the accuracy of the image registration, we use the correlation coefficient (CC) and mutual information (MI) indexes to conduct the quantitative assessment. Both CC and MI can reflect the degree of similarity between two images, and are popular evaluation indexes used in the quality assessment of image registration.

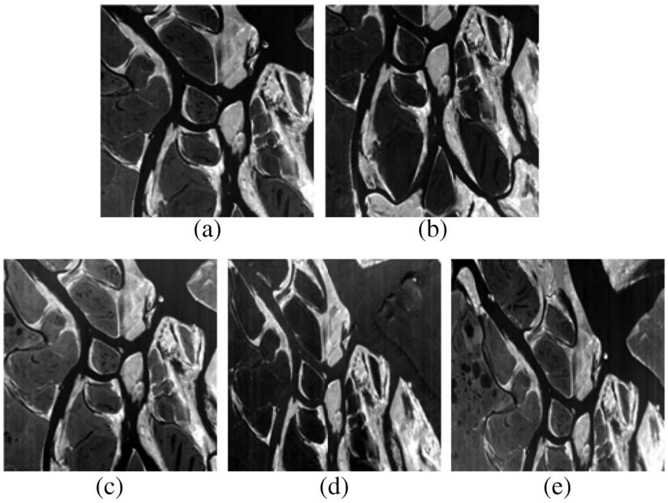
(a) (b)
(c) (d) (e)

Fig. 2. Band 1 of CHRIS_UK (Mode 3) MA-HSI. From (a) to (e): fly-zenith angles are $0°$, $+36°$, $-36°$, $+55°$, and $-55°$.

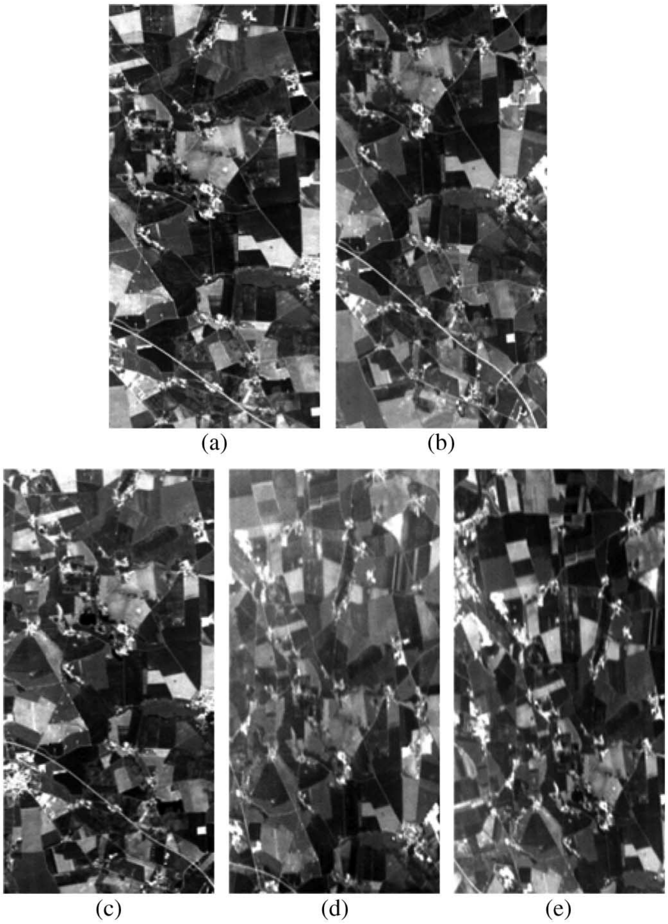
(a) (b)
(c) (d) (e)

Fig. 3. Band 3 of CHRIS_BA (Mode 5) MA-HSI. From (a) to (e): fly-zenith angles are $0°$, $+36°$, $-36°$, $+55°$, and $-55°$.

Let S_i and T_i denote the ith pixel value in the reference and input images, $\overline{S}$ and $\overline{T}$ represent the mean values of the whole

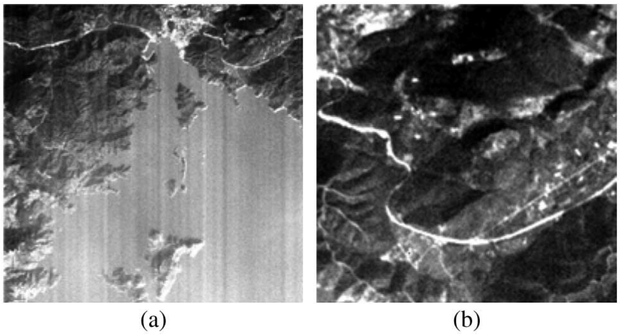

Fig. 4. Some bands polluted by stripe noise or occlusions after preprocessing. (a) Band 2 of CHRIS_FY. (b) Band 3 of CHRIS_BA.

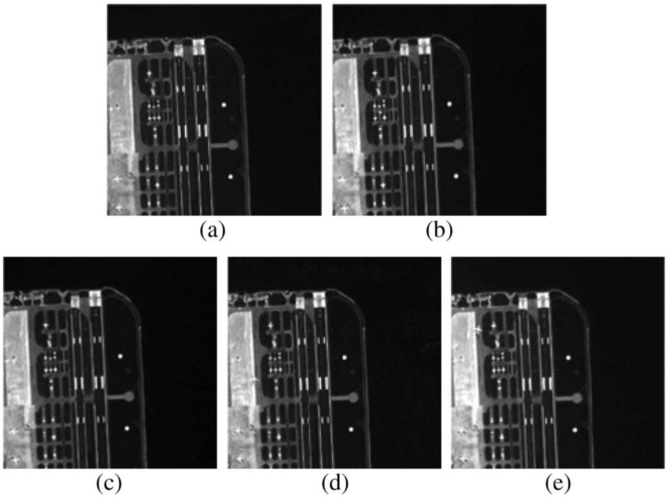

Fig. 5. Band 1 of WV-2 MA-HSI. From (a) to (e): 81.4° in the forward direction; 44.7° in the forward direction; 56.0° in the forward direction; 59.8° in the backward direction; and 44.6° in the backward direction.

images, and N is the number of pixels in the image, then the CC index can be expressed as

$$S_{cc} = \frac{\sum_{i=0}^{N-1}(S_i - \overline{S})(T_i - \overline{T})}{\sqrt{\sum_{i=0}^{N-1}(S_i - \overline{S})^2}\sqrt{\sum_{i=0}^{N-1}(T_i - \overline{T})^2}} \tag{15}$$

where the closer the index is to 1, the higher the registration accuracy is.

For two images A and B the MI index can be defined as

$$I(A,B) = \sum_{a,b} p(a,b)\log\frac{p(a,b)}{p(a)p(b)}. \tag{16}$$

The interpretation of this form is that it measures the distance between the joint distribution of the images' gray values $p(a,b)$ and the joint distribution in the case of independence of the images $p(a)p(b)$. It is a measure of dependence between two images. The assumption is that there is maximal dependence between the gray values of the images when they are correctly aligned. Misregistration will result in a decrease in the measure.

B. Registration Results

In this section, we illustrate the effectiveness of the proposed registration scheme based on the RRRM method. For the CHRIS/Proba images, the 0° angle image is chosen as the reference image, and the remaining four angle images are selected as the sensed ones, i.e., the images to be registered. As for the WorldView-2 images, the image that is closest to the nadir, i.e., 81.4° in the forward direction, is regarded as the reference, and the others are the sensed images.

1) Visual Evaluation: In order to show the details of the registration results, we take a patch as an example in each set of experiments. In order to save space, we only give the registration results of CHRIS_FY for the CHRIS/Proba case and WV-2 for the WorldView-2 case. In the CHRIS_FY case, the size of each patch is 200 × 200 pixels, an overlap of 50 pixels is chosen, and we set the weighting parameter as $\gamma = 0.7$. In the WV-2 case, the same patch size and overlap size is chosen, and the weighting parameter is set as $\gamma = 1.0$.

Fig. 6 shows the patches from CHRIS_FY, where the first row is the nadir patches, i.e. the reference, and the second to the last are the angle patches to be registered. From Fig. 6, it can be seen that some bands are seriously polluted by stripe noise and some pixels are in occlusion. In this situation, the proposed method models these as sparse- and large-magnitude errors, which is represented by E in (6). Consequently, we can still register all the angle patches effectively, as shown in Fig. 7. It is noted that the image coverage areas of the sensed and reference patches are not exactly the same, so the size of the transformed image changes. This leads to the registered patches shown in Fig. 7 having some parts missing, e.g., the first, third, and the last row, which can be seen in the top or bottom of the patches. In addition, some registered angle patches contain all the surface area of the reference patch, e.g., in the second row of Fig. 7, no missing part appears. The registration results of the WV-2 image dataset are shown in Fig. 8, and detailed regions of the registration results are illustrated in Fig. 9. From the perspective of the visual effect, the patches of the large-angle views are well aligned with the nadir one, despite the existence of noise and occlusions. To better show the registration accuracy, in the CHRIS_FY case, we overlay band 4 taken from the three viewing angles after registration with the proposed method to generate a false color composite image, as shown in Fig. 10. The public portions of all the five transformed angle images are cropped out to overlay the display. The red component in the composite refers to the nadir patch, and the other two components refer to two transformed angle patches. It is apparent that no artifacts exist over the entire image, which shows the high quality of our registration results.

Furthermore, we superpose the registered angle image patch with the nadir one, and the two patches of the CHRIS_UK image are stitched together. To highlight the effect of the registration, we select two bands with large differences in pixel intensity. In Fig. 11, the central transition area is obtained by averaging the two patches. To save space, only one large view angle (−55°) patch and one small view angle (−36°) registered patch are provided. Similarly, we can see that the result keeps the consistency in geometry, which verifies the effectiveness of the registration method.

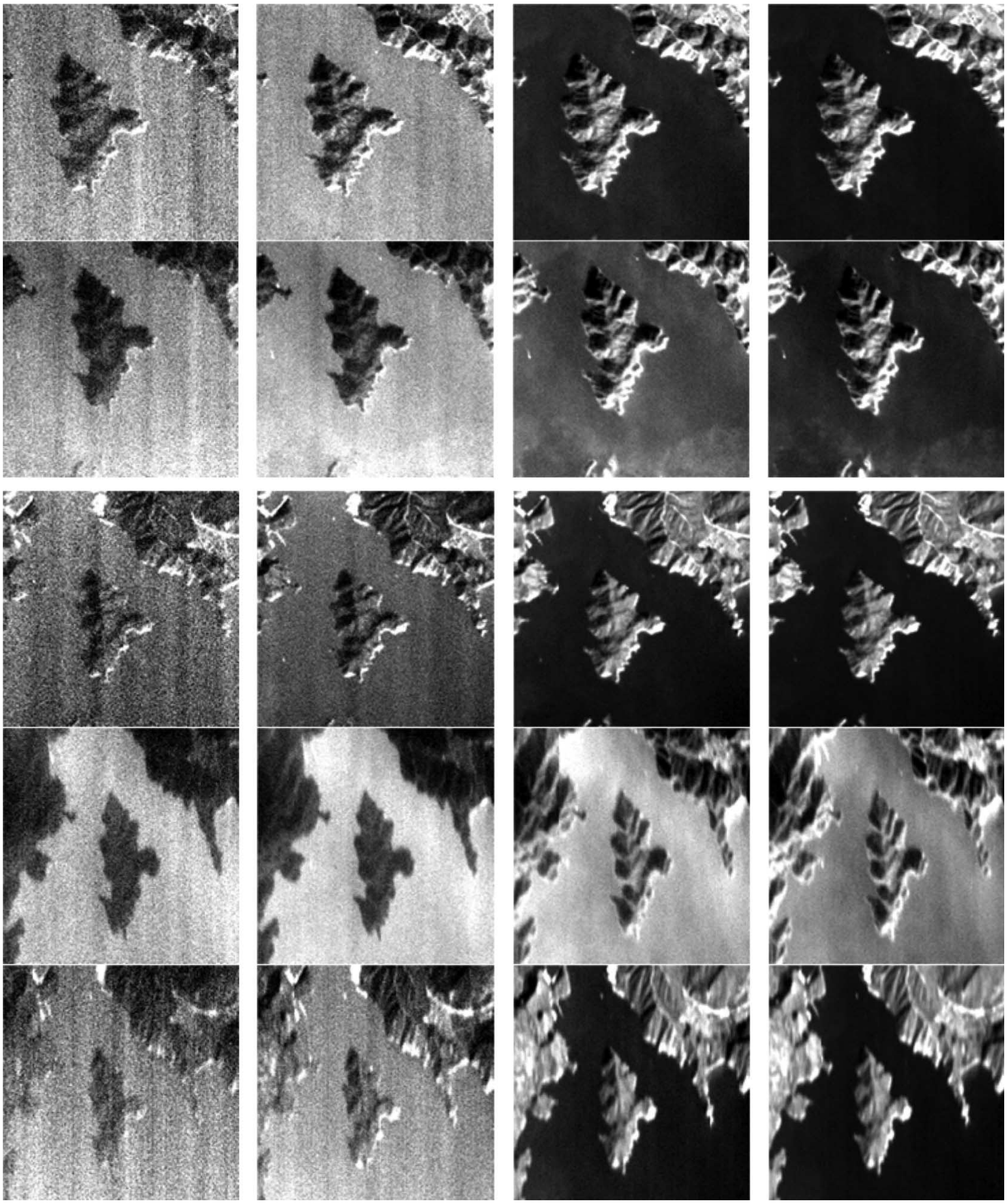

Fig. 6. Patches from CHRIS_FY. From the first row to the last: 0°, $+36^\circ$, -36°, $+55^\circ$, and -55°. Each row shows four different bands, from the first column to the last: bands 1, 2, 5, and 7.

To confirm the superiority of the proposed RRRM method, we use the image registration method proposed in [13], a method based on visual inspection, the traditional SIFT method [9], and the ImReg method [36] as comparative methods. Here, we refer to the method in [13] as $\mathrm{SIFT} + \mathrm{NCC}$, and the method based on visual inspection is referred to as MANUAL. In the MANUAL method, 20 manually selected CPs are used as the ground truth, and a third-order polynomial transformation is adopted. Through our experiments, the third-order polynomial model has proved to be a better model than other global transformation models such as the projective and second-order polynomial models. The experimental results of the MANUAL method change with different sets of CPs, so we perform this experiment three times and select the best result as the result of MANUAL. In the traditional SIFT method, we use the SIFT operator to extract feature points, outliers are eliminated by RANdom SAmple Consensus (RANSAC) [37], and we then adopt a cubic polynomial transformation.

The experimental results show that the SIFT and ImReg methods appear to perform worse than the other three methods. Due to the space constraint, only the experimental results of the RRRM, $\mathrm{SIFT} + \mathrm{NCC}$, and MANUAL methods are shown in Fig. 12, from the first column to the third column, respectively, and the last column shows the reference image. From the image details shown in the red square box, it can be observed that the $\mathrm{SIFT} + \mathrm{NCC}$ method performs worse than the other two methods. This happens mainly because the thin-plate-spline model which the $\mathrm{SIFT} + \mathrm{NCC}$ method adopts is highly dependent on

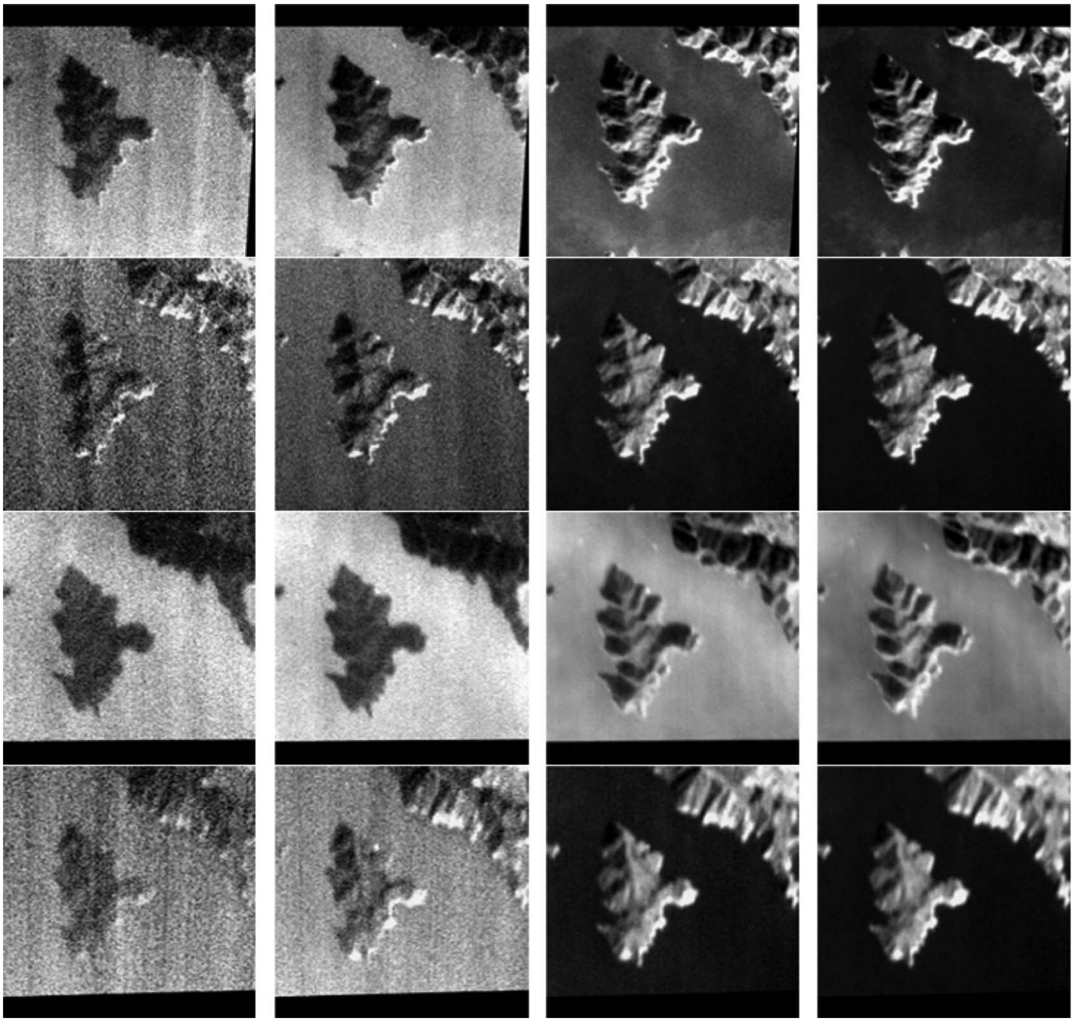

Fig. 7. Transformed patches from CHRIS_FY. From the first row to the last: $+36°$, $-36°$, $+55°$, and $-55°$. Each row shows four different bands, from the first column to the last: bands 1, 2, 5, and 7.

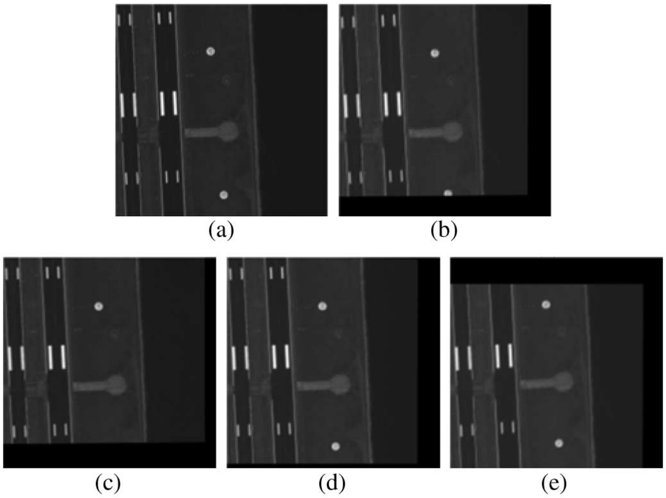

Fig. 8. Registration results for the WV-2 image dataset. (a) Reference patch from band 1. (b)–(e) Four registered angle patches from band 1.

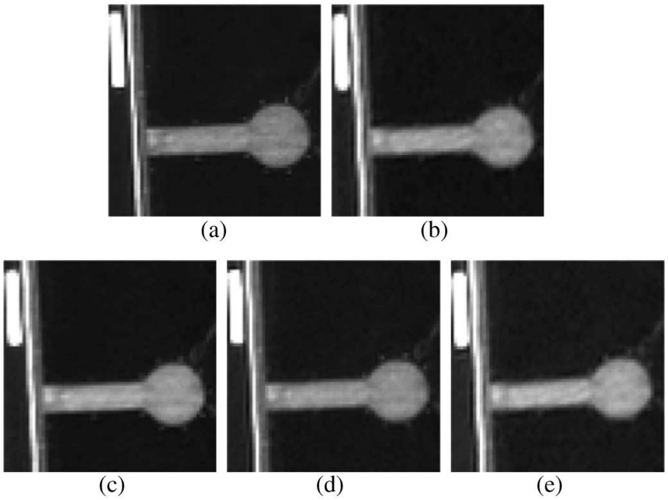

Fig. 9. Detailed regions of the WorldView-2 image registration result. (a) Reference image. (d)–(e) Other four angle images.

the accuracy and amount of CPs, which is usually difficult to obtain for multiangle images, especially large view angle images [38]. In the experimental results of CHRIS_UK, it can be seen that some detailed structural information is lost, which severely reduces the registration quality. From the visual comparison, no obvious differences can be found between the proposed method

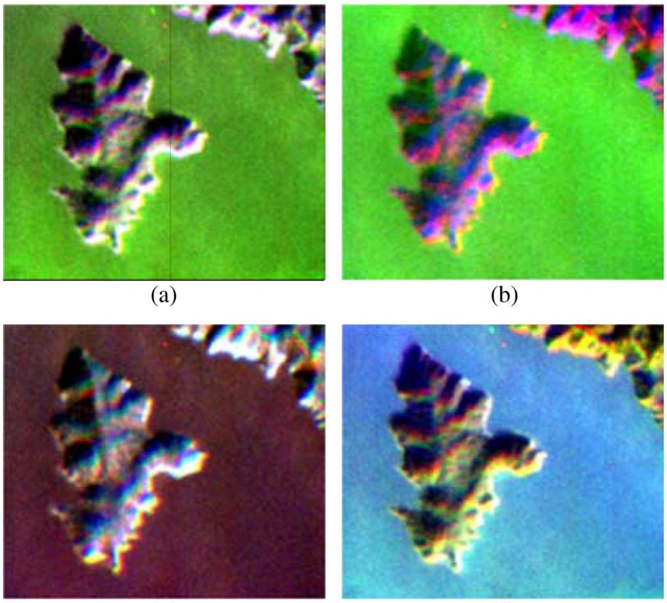
(a) (b) (c) (d)

Fig. 10. Overlay of the band 4 images taken from the three viewing angles after registration in the CHRIS_FY case. From (a) to (d): the composite of 0°, +36°, and −36°; 0°, +55°, and −55°; 0°, −36°, and −55°; and 0°, +36°, and +55°.

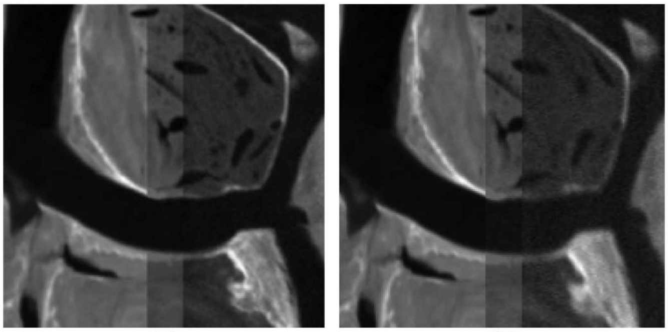
(a) (b)

Fig. 11. Superposition of the registered angle image patch with the nadir one. (a) Band 10 patch from the nadir image and the band 1 patch from the −36° angle image. (b) Band 10 patch from the nadir image and the band 1 patch from the −55° angle image.

and the MANUAL method. From all the above-mentioned comparisons, it can be concluded that the proposed RRRM method outperforms SIFT + NCC and can achieve almost the same effect as the MANUAL method.

2) Quantitative Evaluation: The CC and MI metrics are used to evaluate the quality of the registration images, and the quantitative evaluation results are shown in Tables III and IV. With the use of the patch-based registration scheme, we obtain a series of registered patches. Each patch can then be compared to the reference patch to obtain a corresponding CC value, and we compute the average of these values to represent the accuracy of the entire image.

For each row, the best evaluation result for each image is marked in bold font, and the second-best result is underlined. It is apparent that the traditional SIFT method and the ImReg method perform worse than the other three methods. What is even worse is that sometimes these methods cannot work because no appropriate CP can be found to calculate the transformation, as with the −36° angle image and the +55° angle image of CHRIS_BA. In other words, these two methods are not suitable for multiangle image registration and are not comparable with the other three methods. As for the RRRM, SIFT + NCC, and MANUAL methods, it can be observed that the quantitative evaluation results are consistent with the visual comparisons. The SIFT + NCC method performs badly, especially when applied to the large view angle images. When images are taken from a large view angle, resolution change and blurring make it difficult

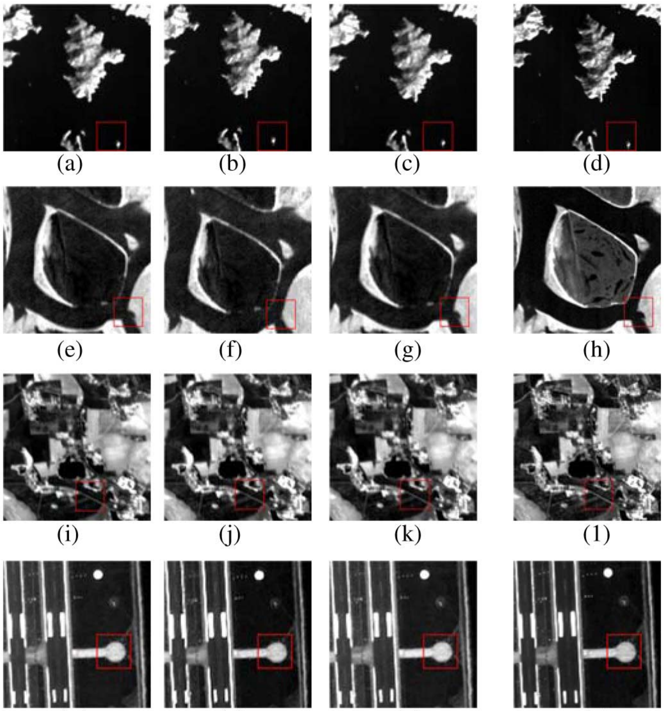
(a) (b) (c) (d)
(e) (f) (g) (h)
(i) (j) (k) (1)
(m) (n) (o) (p)

Fig. 12. Details of the registration results by the different methods. From the first row to the last: CHRIS_FY, CHRIS_UK, CHRIS_BA, and WV-2, respectively. From the first column to the last: RRRM, SIFT + NCC, MANUAL, and the reference image, respectively.

TABLE III
COMPARISON OF CC AMONG DIFFERENT METHODS

Site	Angle	RRRM	SIFT+ NCC	SIFT	ImReg	MANUAL
CHR IS_ FY	+36°	**0.9714**	0.9306	0.8321	0.8412	0.9546
	−36°	**0.9783**	0.9278	0.8415	0.8307	0.9659
	+55°	**0.9739**	0.9073	0.8097	–	0.9179
	−55°	**0.9685**	0.9141	0.8140	0.8001	0.9482
CHR IS_ UK	+36°	**0.9736**	0.9364	0.8346	0.8917	0.9589
	−36°	**0.9780**	0.9385	0.8321	0.8642	0.9667
	+55°	**0.9687**	0.9026	0.8179	0.8482	0.9191
	−55°	**0.9779**	0.9240	0.8162	0.8361	0.9434
CHR IS_ BA	+36°	0.9723	0.9341	0.8413	0.8503	**0.9857**
	−36°	**0.9764**	0.9370	0.8391	–	0.9618
	+55°	0.9737	0.9066	0.8115	–	**0.9788**
	−55°	**0.9693**	0.9135	0.8094	0.8286	0.9653
WV -2	+44.7°	**0.9924**	0.9651	0.9167	0.9286	0.9912
	+56.0°	**0.9903**	0.9723	0.9107	0.9284	0.9881
	−59.8°	**0.9895**	0.9764	0.9136	0.9366	0.9894
	−44.6°	**0.9889**	0.9754	0.9170	0.9342	0.9847

TABLE IV
COMPARISON OF MI AMONG DIFFERENT METHODS

Site	Angle	RRRM	SIFT+ NCC	SIFT	ImReg	MANUAL
CHRIS_FY	+36°	**1.5712**	1.3987	1.2006	1.2609	1.5659
	−36°	**1.6059**	1.5255	1.3112	1.3218	1.5259
	+55°	**1.5759**	1.4807	1.2726	–	1.4547
	−55°	**1.5948**	1.4789	1.2238	1.2242	1.5726
CHRIS_UK	+36°	**1.6015**	1.4956	1.2601	1.3269	1.5398
	−36°	**1.6278**	1.5701	1.3132	1.3567	1.5945
	+55°	**1.6017**	1.5201	1.2363	1.2609	1.5904
	−55°	**1.6059**	1.5311	1.3028	1.3582	1.5535
CHRIS_BA	+36°	1.8023	1.7731	1.4768	1.4520	**1.8230**
	−36°	**1.8235**	1.7568	1.4456	–	1.8141
	+55°	1.8121	1.7049	1.5124	–	**1.8206**
	−55°	**1.8159**	1.6414	1.5021	1.5219	1.8135
WV-2	+44.7°	**1.8175**	1.7521	1.5968	1.6042	1.8168
	+56.0°	1.8235	1.7832	1.6001	1.6125	**1.8241**
	−59.8°	**1.8383**	1.7981	1.6249	1.6417	1.8362
	−44.6°	**1.8171**	1.7873	1.6036	1.6124	1.8159

TABLE V
COMPARISON OF THE REGISTRATION ACCURACY WITH DIFFERENT PATCH SIZES AND OVERLAP SIZES

		CC			MI		
		CHRIS_FY	CHRIS_UK	CHRIS_BA	CHRIS_FY	CHRIS_UK	CHRIS_BA
100	25%	0.9652	0.9684	0.9606	1.5996	1.5983	1.7852
	45%	0.9730	0.9761	0.9718	1.6005	1.5986	1.7906
	65%	0.9739	0.9733	0.9754	**1.6229**	1.6082	1.7997
150	25%	0.9757	0.9653	0.9647	1.5987	1.6128	1.7981
	45%	0.9789	0.9722	0.9660	1.6092	**1.6273**	1.7995
	65%	**0.9792**	**0.9786**	0.9675	1.6015	1.6250	1.7995
200	25%	0.9714	0.9736	0.9723	1.5712	1.6015	1.8023
	45%	0.9726	0.9698	0.9756	1.5786	1.6111	**1.8116**
	65%	0.9725	0.9651	**0.9760**	1.5780	1.6238	1.8109
250	25%	0.9682	0.9551	0.9730	1.5734	1.6003	1.8045
	45%	0.9697	0.9530	0.9739	1.5237	1.6015	1.8116
	65%	0.9688	0.9535	0.9746	1.5703	1.6022	1.8087
300	25%	0.9512	0.9439	0.9647	1.5644	1.5936	1.7812
	45%	0.9536	0.9476	0.9635	1.5685	1.5981	1.7826
	65%	0.9504	0.9484	0.9633	1.5579	1.5998	1.7831

to extract enough CPs of high quality, leading to the relatively low registration accuracy. In addition, $\mathrm{SIFT} + \mathrm{NCC}$ only works well in areas with little variation in topography, and this requirement cannot always be met in actual situations. For example, there is obvious elevation variation in the CHRIS_FY image.

Comparing the RRRM method with the MANUAL method, it can be seen that RRRM generally achieves better results in all four experiments, which proves that the proposed RRRM method works well for MA-HSI-MSI, without manual intervention. Viewpoint changes and varying illumination also result in some weakness in the MANUAL registration procedure, leading to the result being unstable. CP selection remains a challenge due to the phenomenon of resolution change and blurring. For example, in the CHRIS_UK experiment, good results are achieved for the small view angle ($+36^\circ$ and -36°) images, but unsatisfactory results are obtained for the large ones ($+55^\circ$ and -55°). Nevertheless, this disadvantage can be overcome in the proposed RRRM method because the feature extraction step of the traditional registration methods is cleverly avoided. Meanwhile, no such obvious difference exists between the large-angle views and the small-angle views, because they are treated in a unified framework. It should also be mentioned that the proposed RRRM method is robust with regard to noise and occlusions, which often exist within multiangle imagery, even after preprocessing.

It is possible to handle all the angle images and all the bands in a single RRRM procedure, which makes the solved set of transformations for the four angle images globally optimal. However, in the comparative methods, only one or three bands/components of good visual quality are used to select the CPs and then registered with their optimal transformation, which lowers the performance and robustness of these methods [39]. In addition, with the traditional methods, only one angle image is dealt with during each registration procedure, with respect to the reference image, and the registration result is only optimal for the image pair. However, this will obviously not be optimal for all the angle images, because of the pairwise error transfer or accumulation. From this perspective, the RRRM registration method outperforms the other methods because all five angle images are used at the same time.

3) Patch and Overlap Size Analysis: As mentioned in Section I, local distortion exists in multiangle images, which means that a global transformation model is not appropriate for the whole image. If the patch size is large, the homography transformation will also not be suitable. On the other hand, if the patch size is relatively small, the number of image patches and the time cost will increase accordingly. Similarly, if the size of the overlap is large, the time cost will again be high.

Here, we use CHRIS/Proba images to analyze the effect of patch and overlap size. A series of experiments is conducted with the patch size varying from 100 to 300 pixels, with a step of 50 pixels, and the overlap size varying from 25% to 65% of the corresponding patch size, with a step of 20%. We take the $+36^\circ$ angle image as an example to analyze the effect of the size of the patch and the size of the overlap on the registration result. Table V shows the registration accuracy with different patch sizes and overlap sizes, in terms of CC and MI. The quantitative evaluation results for each multiangle image dataset are given in each column of the table, in which the optimal results are labeled in bold and the next seven suboptimal results are underlined. To clearly illustrate the sensitivity of the RRRM method with regard to the patch size and overlap size, we show the change curve of the CC index with regard to different patch sizes and overlap sizes in Fig. 13.

From Table V, it can be clearly observed that a reasonable patch size falls in the range of [100, [250]. From Fig. 13, it can be seen that the registration accuracy first begins to increase as the patch size increases. Then, when the patch size reaches a certain value, the registration accuracy begins to gradually decline. For the overlap size, it can be generally observed that the registration accuracy reaches its optimal when the overlap size is set as 65% of the patch size. Furthermore, it can be seen that the effect of the overlap size on the image registration accuracy is relatively small. Considering all these factors, the size of the image patch and the size of the overlap are set as 200 and 50 in this paper, respectively.

4) Parameter Analysis: The weighting parameter γ trades off the rank of the solution versus the sparsity of the gross errors. The theoretical analysis in [25] suggests that the weighting parameter γ should be of the form $C/\sqrt{m}$, where C is a constant, typically set to around unity, and m is the number of pixels in each patch.

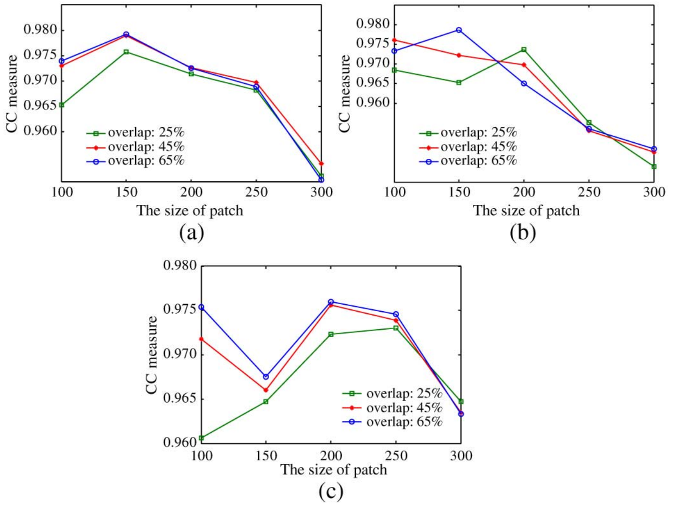

(a) (b) (c)

Fig. 13. Sensitivity analysis of the patch size and overlap size. (a) Change curve of the CC measure when the patch size or overlap size varies for CHRIS_FY. (b) Change curve of the CC measure when the patch size or overlap size varies for CHRIS_UK. (c) Change curve of the CC measure when the patch size or overlap size varies for CHRIS_BA.

To acquire the optimal value of the weighting parameter, we conduct a series of experiments using the CHRIS/Proba images, with a range of [0.1, 1.5] and a step size of 0.1. Fig. 14 shows the sensitivity of the weighting parameter for different image datasets.

It can be seen that the optimal value of the weighting parameter is closely related to the image content and is not fixed for different image datasets. It is therefore a difficult task to give an optimal value or an adaptive determination method for the weighting parameter γ, the value of which is obtained empirically in this paper. For CHRIS_UK, the magnitude of the CC value change is much larger than for the other two datasets over the parameter range of [0.1, 1.5]. As γ increases from 0.1, the CC value first rises. Then, when the growth reaches a certain level, it arrives at the maximum and begins to show a downward trend, which happens in all three experiments. The optimal value of γ for the CHRIS_FY, CHRIS_UK, and CHRIS_BA images is about 0.7, 1.0, and 0.8, respectively. As the main focus of this paper is the formation of the proposed RRRM image registration method for MA-HSI-MSI, the adaptive selection of weighting parameter is out of the scope of this paper, but will be investigated in our future work. Through a number of experiments, it can be observed that when the value of the parameter γ is within the range of [0.6, 1.2], the registration performance of the proposed RRRM method is relatively stable. Therefore, the range of [0.6, 1.2] is recommended for the selection of parameter γ. Furthermore, the registration accuracy of large view angle images is almost always lower than for small-angle images. However, when the optimal weighting parameter γ is chosen, the registration accuracy difference between large view angle images and small-angle images is relatively small.

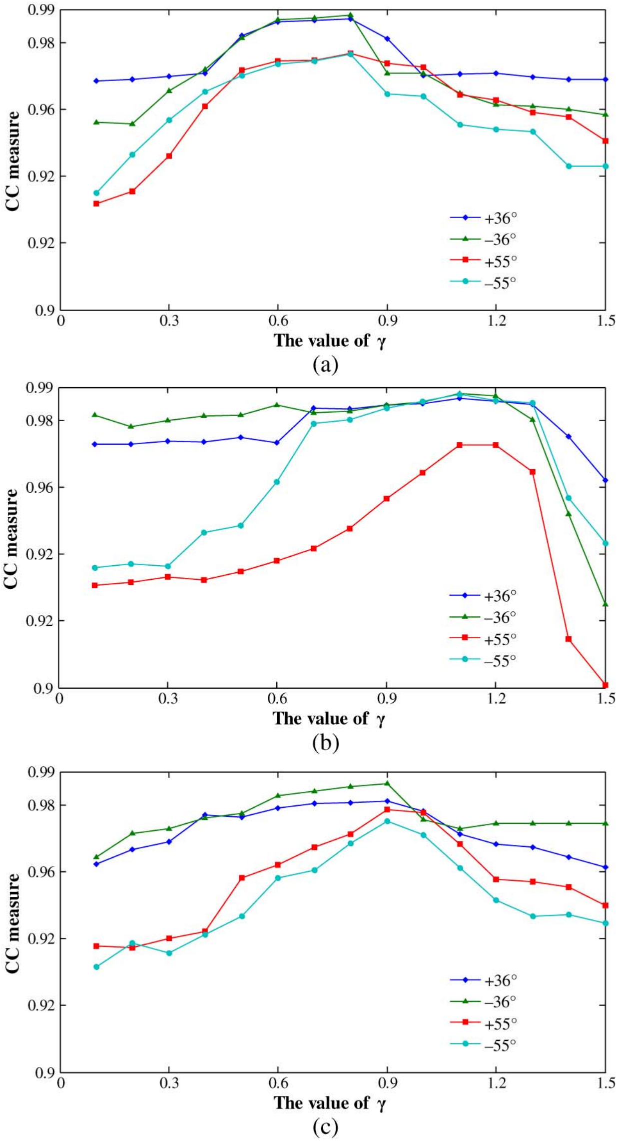

(a) (b) (c)

Fig. 14. Sensitivity analysis for the weighting parameter γ. (a) Corresponding change in the CC measure when γ varies for CHRIS_FY. (b) Corresponding change in the CC measure when γ varies for CHRIS_UK. (c) Corresponding change in the CC measure when γ varies for CHRIS_BA.

TABLE VI
TIMES COST FOR EACH DATASET WITH DIFFERENT VALUES OF γ

	0.1	0.5	0.9	1.2	1.5	Average
CHRIS_FY	30.2	31.8	28.3	28.0	30.8	29.5
CHRIS_UK	35.1	35.4	37.5	36.5	35.7	34.9
CHRIS_BA	41.7	41.8	42.5	43.0	42.1	42.9

5) Time Cost and Convergence Analysis: The time cost of the proposed RRRM image registration method is investigated in this section. We calculate the time cost of the patch set for each multiangle CHRIS/Proba image dataset, with different selections of the weighting parameter γ. To save space, only the time costs of five different γ values are listed in Table VI, and the last column denotes the average time cost, with γ varying from 0.1 to 1.5. The experiments were conducted in MATLAB R2011b on a 3.07 GHz Intel Core i3 machine with 6.0 GB RAM. Overall, it can be observed that the time cost falls in an acceptable range. Furthermore, it is also reasonable to believe that with the rapid development in computer hardware and computation techniques, the time cost will soon no longer be an issue.

The convergence property of the proposed RRRM image registration method is also investigated. The convergence curves

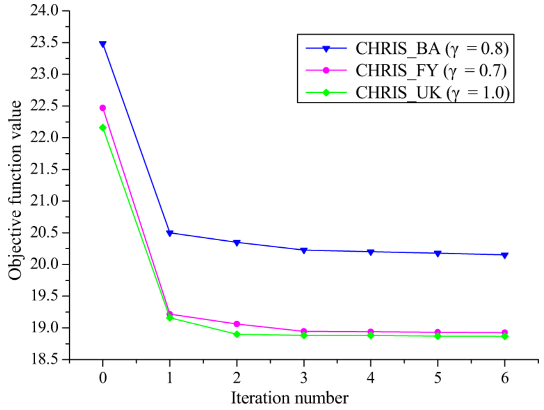

Fig. 15. Convergence analysis of the proposed RRRM method.

TABLE VII
DECREASE OF THE OBJECTIVE FUNCTION VALUE

Methods	Iteration 0	Iteration 1	Iteration 2	Iteration 3	Iteration 4	Iteration 5	Iteration 6
Harris	22.4685	19.2172	19.0631	18.9452	18.9057	18.8991	18.8968
SUSAN	22.5021	19.2261	19.0663	18.9456	18.9197	18.9093	18.8988
SIFT	22.3512	19.2060	19.0763	18.9314	18.8967	18.8952	18.8931
SURF	22.3578	19.2137	19.0832	18.9250	18.9001	18.8957	18.8934

of the three multiangle CHRIS/Proba image datasets, CHRIS_FY, CHRIS_UK, and CHRIS_BA, are illustrated in Fig. 15. It can be observed that the objective function value of (10) decreases with the iterations and then finally achieves a stable level, which suggests the convergence of the proposed RRRM method. It should also be noted that the images have been normalized in the initialization step of Algorithm 1, which leads to the objective function value being relatively low.

Furthermore, the sensitivity analysis of the proposed RRRM method with respect to the initialization is given here to deepen the understanding of its convergence. We conduct an experiment using the CHRIS_FY image set. In the experiment, the initialization is obtained using four different feature extraction operators, i.e., Harris, SUSAN, SIFT, and SURF. The sensitivity of the RRRM algorithm to the initialization is analyzed in terms of the decrease of objective function value and the image registration accuracy measures.

From Table VII, it can be found that the initial objective function value varies in a small range and the final value reaches almost the same level, which shows that the almost identical registration accuracy is obtained. The CC and MI values of the registration images under different initializations are given in Table VIII. Clearly, the variation of registration accuracy is consistent with the decrease of objective function value. Therefore, it can be concluded that different initializations would lead to almost the same registration results and the registration accuracy stays in a reasonable range as long as the initialization is relatively suitable.

TABLE VIII
COMPARISONS OF CC AND MI INDEXES UNDER DIFFERENT INITIALIZATIONS

	CC				**MI**			
	+36°	–36°	+55°	–55°	+36°	–36	+55°	–55°
Harris	0.9714	0.9783	0.9739	0.9685	1.5712	1.6059	1.5759	1.5948
SUSAN	0.9700	0.9779	0.9729	0.9677	1.5707	1.6054	1.5755	1.5945
SIFT	0.9723	0.9801	0.9745	0.9694	1.5720	1.6065	1.5767	1.5957
SURF	0.9722	0.9802	0.9743	0.9695	1.5721	1.6064	1.5766	1.5957

TABLE IX
COMPARISON OF RRRM AND SIFT + NCC METHODS UNDER DIFFERENT GAUSSIAN NOISE LEVELS

	CC		MI	
SNR value	RRRM	SIFT+NCC	RRRM	SIFT+NCC
5.09 dB	0.9651	0.8004	1.6172	1.1751
8.27 dB	0.9690	0.8312	1.6224	1.2945
10.78 dB	0.9726	0.8642	1.6318	1.3440
13.47 dB	0.9745	0.8973	1.6326	1.3916
16.52 dB	0.9776	0.9107	1.6335	1.4682

TABLE X
COMPARISON OF RRRM AND SIFT + NCC METHODS UNDER DIFFERENT IMPULSE NOISE LEVELS

	CC		MI	
Noise density	RRRM	SIFT+NCC	RRRM	SIFT+NCC
18.86%	0.9638	0.6923	1.6103	0.9816
15.07%	0.9643	0.7463	1.6127	1.1513
12.98%	0.9672	0.7840	1.6155	1.2405
9.25%	0.9739	0.7971	1.6223	1.2908
7.43%	0.9756	0.8469	1.6231	1.3251
5.89%	0.9775	0.8854	1.6239	1.4426

6) Analysis of the Effect of Noise: This section investigates the effect of noise on the proposed RRRM image registration method. The CHRIS_UK image dataset is chosen to conduct the simulation experiment because it can be viewed as almost clean, without any noise. In this simulated experiment, two kinds of noise are added to the CHRIS_UK image. The first kind is zero-mean Gaussian noise, with the SNR value of each band varying from 0 to 20 dB, and the second type is impulse noise, with the percentage of contaminated part varying from 0% to 20%. The quantitative experimental results of the simulation images with both Gaussian and impulse noise are shown in Tables IX and X, respectively. From the two tables, it can be clearly observed that the performance of the SIFT + NCC method drops with the increase of noise level. When noise exists, the SIFT + NCC method is severely affected or even do not work, whereas the RRRM method can model all these obstacles as sparse gross errors and suppress their negative effect in the registration process. Therefore, the superiority of the RRRM model stands evidently in the presence of noise.

V. CONCLUSION

Multiangle imagery provides directional reflectance properties of the earth's surface; however, its registration is faced with challenges due to the large view angles. This paper proposes an

RRRM for MA-HSI-MSI. By exploiting the low-rank structure of the MA-HSI-MSI, the proposed RRRM method cleverly avoids the deficiency of multiangle image feature extraction. In addition, we adopt a patch-based registration strategy to tackle the problem of local geometric distortion. Specifically, the entire images are divided into several patches with a certain overlap, and we find the optimal homography transformation to represent the local distortion. All the bands of the multiangle images participate in a single registration procedure, which makes the proposed method robust with regard to stripes and occlusions. The proposed RRRM method was tested on three CHRIS/Proba image datasets and a WorldView-2 dataset. Overall, the extensive experimental results clearly show that the proposed RRRM method achieves a superior registration performance.

However, there is still some room for improvement of the proposed method. For example, adaptive selection of the weighting parameter needs further investigation. Another interesting issue is the type of transformation model: parametric smooth transformation could be used to handle more challenging earth surfaces, instead of homography transformation.

ACKNOWLEDGMENT

The authors would like to thank the handling editor and anonymous reviewers for their careful reading and helpful remarks. They also thank DigitalGlobe for providing the WorldView-2 scenes from Rio de Janeiro for the IEEE-IGARSS 2011 Data Fusion Contest.

REFERENCES

[1] A. E. Galbraith, J. Theiler, K. J. Thome, and R. W. Ziolkowski, "Resolution enhancement of multilook imagery for the multispectral thermal imager," *IEEE Trans. Geosci. Remote Sens.*, vol. 43, no. 9, pp. 1964–1977, Sep. 2005.

[2] M. Chopping, L. Su, A. Laliberte, A. Rango, D. P. Peters, and N. Kollikkathara, "Mapping shrub abundance in desert grasslands using geometric-optical modeling and multi-angle remote sensing with CHRIS/Proba," *Remote Sens. Environ.*, vol. 104, no. 1, pp. 62–73, Sep. 2006.

[3] H. Zhang, Z. Yang, L. Zhang, and H. Shen, "Super-resolution reconstruction for multi-angle remote sensing images considering resolution differences," *Remote Sens.*, vol. 6, pp. 637–657, Jan. 2014.

[4] L. Alonso and J. Moreno, "Advances and limitations in a parametric geometric correction of CHRIS/Proba data," in *Proc. 3rd CHRIS/Proba Workshop,* Frascati, Italy, Mar. 21–23, 2005, pp. 5–11.

[5] M. Kneubühler, B. Koetz, R. Richter, M. Schaepman, and K. Itten, "Geometric and radiometric pre-processing of CHRIS/PROBA data over mountainous terrain," in *Proc. 3rd CHRIS/PROBA Workshop,* Frascati, Italy, Mar. 21–23, 2005, pp. 54–59.

[6] A. Goshtasby, "Registration of images with geometric distortions," *IEEE Trans. Geosci. Remote Sens.*, vol. 26, no. 1, pp. 60–64, Jan. 1988.

[7] Y. Huachao, Z. Shubi, and W. Yongbo, "Robust and precise registration of oblique images based on scale-invariant feature transformation algorithm," *IEEE Geosci. Remote Sens. Lett.*, vol. 9, no. 4, pp. 1–5, Jul. 2012.

[8] Z. Zhang, A. Ganesh, X. Liang, and Y. Ma, "Tilt: Transform invariant low-rank textures," *Int. J. Comput. Vis.*, vol. 99, no. 1, pp. 1–14, Aug. 2012.

[9] D. G. Lowe, "Distinctive image features from scale-invariant keypoints," *Int. J. Comput. Vis.*, vol. 60, no. 2, pp. 91–110, Nov. 2004.

[10] G. Yu and J. Morel, "A fully affine invariant image comparison method," in *Proc. IEEE Int. Conf. Acoust., Speech Signal Process.* (ICASSP'09), 2009, pp. 1597–1600.

[11] J. Ma, J. C.-W. Chan, and F. Canters, "Automatic image registration of multi-angle imagery for CHRIS/Proba," in *Proc. 6th EARSeL SIG IS Workshop,* Tel Aviv, Israel, Mar. 16–19, 2009, pp. 27–33 [CD-ROM], .

[12] S. Leprince, S. Barbot, F. Ayoub, and J. P. Avouac, "Automatic and precise orthorectification, coregistration, and subpixel correlation of satellite images, application to ground deformation measurements," *IEEE Trans. Geosci. Remote Sens.*, vol. 45, no. 6, pp. 1529–1558, Jun. 2007.

[13] J. Ma, J. C.-W. Chan, and F. Canters, "Fully automatic subpixel image registration of multiangle CHRIS/Proba data," *IEEE Trans. Geosci. Remote Sens.*, vol. 48, no. 7, pp. 2829–2839, Jul. 2010.

[14] J. M. Morel and G. Yu, "ASIFT: A new framework for fully affine invariant image comparison," *SIAM J. Imag. Sci.*, vol. 2, no. 2, pp. 438–469, Apr. 2009.

[15] S. M. H. Anvar, W.-Y. Yau, and E. K. Teoh, "Multi-view face detection and registration requiring minimal manual intervention," *IEEE Trans. Pattern Anal. Mach. Intell.*, vol. 35, no. 10, pp. 2484–2497, Oct. 2013,.

[16] B. Zitova and J. Flusser, "Image registration methods: A survey," *Image Vis. Comput.*, vol. 21, no. 11, pp. 977–1000, Oct. 2003.

[17] Y. Peng, A. Ganesh, J. Wright, W. Xu, and Y. Ma, "RASL: Robust alignment by sparse and low-rank decomposition for linearly correlated images," in *Proc. IEEE Conf. Comput. Vis. Pattern Recognit.* (CVPR'10), Jun. 13–18, 2010, pp. 763–770.

[18] L. Wang, Y. Sun, S. Gao, and S. Zhao, "Automatic misalignment correction of seismograms using low-rank matrix recovery," *IEEE Geosci. Remote Sens. Lett.*, vol. 10, no. 2, pp. 352–356, Mar. 2013.

[19] Y. Wu, B. Shen, and H. Ling, "Online robust image alignment via iterative convex optimization," in *Proc. IEEE Conf. Comput. Vis. Pattern Recognit.* (CVPR'12), 2012, pp. 1808–1814.

[20] H. Abdi and L. J. Williams, "Principal component analysis," *Wiley Interdiscip. Rev. Comput. Stat.*, vol. 2, no. 4, pp. 433–459, 2010.

[21] M. Journée, Y. Nesterov, P. Richtárik, and R. Sepulchre, "Generalized power method for sparse principal component analysis," *J. Mach. Learn. Res.*, vol. 11, pp. 1–30, Feb. 2010.

[22] A. Ifarraguerri and C.-I. Chang, "Multispectral and hyperspectral image analysis with convex cones," *IEEE Trans. Geosci. Remote Sens.*, vol. 37, no. 2, pp. 756–770, Mar. 1999.

[23] C. Li, T. Sun, K. F. Kelly, and Y. Zhang, "A compressive sensing and unmixing scheme for hyperspectral data processing," *IEEE Trans. Image Process.*, vol. 21, no. 3, pp. 1200–1210, Mar. 2012.

[24] H. Zhang, W. He, L. Zhang, H. Shen, and Q. Yuan, "Hyperspectral image restoration using low-rank matrix recovery," *IEEE Trans. Geosci. Remote Sens.*, vol. 52, no. 8, pp. 4729–4743, Oct. 2013.

[25] M. Golbabaee and P. Vandergheynst, "Hyperspectral image compressed sensing via low-rank and joint-sparse matrix recovery," in *Proc. IEEE Int. Conf. Acoust., Speech Sig. Process.* (ICASSP), Mar. 25–30, 2012, pp. 2741–2744.

[26] M. Jianglin, J. C. W. Chan, and F. Canters, "An operational superresolution approach for multi-temporal and multi-angle remotely sensed imagery," *IEEE J. Sel. Topics Appl. Earth Observ. Remote Sens.*, vol. 5, no. 1, pp. 110–124, Dec. 2012.

[27] D. Conrad and G. DeSouza, "Homography-based ground plane detection for mobile robot navigation using a modified EM algorithm," in *Proc. IEEE Int. Conf. Robot. Autom.* (ICRA), May 3–7, 2010, pp. 910–915.

[28] J. Wright, A. Ganesh, S. Rao, and Y. Ma, "Robust principal component analysis: Exact recovery of corrupted low-rank matrices," in *Proc. Neural Inf. Process. Sys.* (NIPS), Dec. 2009, pp. 1–9.

[29] Z. Zhou, X. Li, J. Wright, E. Candes, and Y. Ma, "Stable principal component pursuit," in *Proc. IEEE Int. Symp. Inf. Theory* (ISIT), 2010, pp. 1518–1522.

[30] M. Fazel, "Matrix rank minimization with applications," Ph.D. dissertation, Elect. Eng. Dep., Stanford Univ., Stanford, CA, USA, 2002.

[31] K. Jittorntrum and M. Osborne, "Strong uniqueness and second order convergence in nonlinear discrete approximation," *Numer. Math.*, vol. 34, no. 4, pp. 439–455, 1980.

[32] D. L. Donoho and C. Grimes, "Image manifolds which are isometric to Euclidean space," *J. Math. Imaging Vis.*, vol. 23, no. 1, pp. 5–24, 2005.

[33] J. Garcia and J. Moreno, "Removal of noises in CHRIS/Proba images: Application to the SPARC campaign data," in *Proc. 2nd CHRIS/Proba Workshop,* Frascati, Italy, Apr. 28–30, 2004, pp. 23–27.

[34] The ESA Envisat Project, BEAM Software [Online]. Available: http://www.brockmann-consult.de/cms/web/beam/releases

[35] L. Guanter, L. Alonso, and J. Moreno, "A method for the surface reflectance retrieval from PROBA/CHRIS data over land: Application to ESA SPARC campaigns," *IEEE Trans. Geosci. Remote Sens.*, vol. 43, no. 12, pp. 2908–2917, Dec. 2005.

[36] Vision Research Lab, ECE, University of California Santa Barbara. imREG Software [Online]. Available: http://vision.ece.ucsb.edu/registration/demo/

[37] M. A. Fischler and R. C. Bolles, "Random sample consensus: A paradigm for model fitting with applications to image analysis and automated cartography," *Commun. ACM*, vol. 24, pp. 381–395, 1981.

[38] F. L. Bookstein, "Principal warps: Thin-plate splines and the decomposition of deformations," *IEEE Trans. Pattern Anal. Mach. Intell.*, vol. 11, no. 6, pp. 567–585, Jun. 1989.

[39] H. Zhang, L. Zhang, and H. Shen, "A super-resolution reconstruction algorithm for hyperspectral images," *Sig. Process.*, vol. 92, no. 9, pp. 2082–2096, 2012.

Ting Hu received the B.S. degree in remote sensing science and technology from Wuhan University, Wuhan, China, in 2012. She is currently pursuing the M.S. degree at the State Key Laboratory of Information Engineering in Surveying, Mapping and Remote Sensing (LIESMARS), Wuhan University.

Her research interests include image registration and super-resolution in multiangle remote sensing images.

Hongyan Zhang (M'13) received the Ph.D. degree in remote sensing from Wuhan University, Wuhan, China, in 2010.

Since 2010, he has been a Lecturer with the State Key Laboratory of Information Engineering in Surveying, Mapping, and Remote Sensing, Wuhan University. His research interests include image reconstruction, sparse representation, and low-rank methods for sensing image imagery.

Dr. Zhang is a Reviewer of several international academic journals, including IEEE TRANSACTION ON GEOSCIENCE AND REMOTE SENSING, IEEE TRANSACTION ON IMAGE PROCESSING, IEEE *Journal of Selected Topics in Applied Earth Observations and Remote Sensing*, IEEE GEOSCIENCE AND REMOTE SENSING LETTERS, and so on.

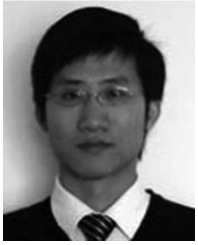

Huanfeng Shen (M'11–SM'13) received the B.S. degree in surveying and mapping engineering and the Ph.D. degree in photogrammetry and remote sensing both from Wuhan University, Wuhan, China, in 2002 and 2007, respectively.

In July 2007, he joined the School of Resource and Environmental Science, Wuhan University, where he is currently a Full Professor. He has published more than 60 research papers. His research interests include image processing (for quality improvement), remote sensing application, data fusion, and assimilation.

Dr. Shen has been supported by several talent programs, including the New Century Excellent Talents by the Ministry of Education of China (2011) and the Hubei Science Fund for Distinguished Young Scholars (2011).

Liangpei Zhang (M'06–SM'08) received the B.S. degree in physics from Hunan Normal University, ChangSha, China, the M.S. degree in optics from the Xi'an Institute of Optics and Precision Mechanics, Chinese Academy of Sciences, Xi'an, China, and the Ph.D. degree in photogrammetry and remote sensing from Wuhan University, Wuhan, China, in 1982, 1988, and 1998, respectively.

He is currently the Head of the Remote Sensing Division, State Key Laboratory of Information Engineering in Surveying, Mapping, and Remote Sensing, Wuhan University. He is also a "Chang-Jiang Scholar" Chair Professor appointed by the Ministry of Education, China. He is now a Principal Scientist for the China State Key Basic Research Project (2011–2016) appointed by the Ministry of National Science and Technology of China to lead the remote sensing program in China. He has more than 260 research papers and is the holder of 5 patents. His research interests include hyperspectral remote sensing, high resolution remote sensing, image processing, and artificial intelligence.

Dr. Zhang regularly serves as a Co-Chair of the series Society of Photo-Optical Instrumentation (SPIE) Engineers Conferences on Multispectral Image Processing and Pattern Recognition (MIPPR), Conference on Asia Remote Sensing, and many other conferences. He also serves as an Associate Editor of IEEE TRANSACTIONS ON GEOSCIENCE AND REMOTE SENSING, *International Journal of Ambient Computing and Intelligence* (IJACI), *International Journal of Image and Graphics*, *International Journal of Digital Multimedia Broadcasting*, *Journal of Geo-spatial Information Science*, and the *Journal of Remote Sensing*. He is a Fellow of the Institution of Engineering and Technology (IET), and Executive Member (Board of Governor) of the China National Committee of International Geosphere-Biosphere Programme.